

Advanced Electrode Materials Comprising of Structure-Engineered Quantum Dots for High-Performance Asymmetric Micro-Supercapacitors

Wenwen Liu, Maiwen Zhang, Matthew Li, Brenda Li, Wenyao Zhang, Gaoran Li, Meiling Xiao, Jianbing Zhu, Aiping Yu,* and Zhongwei Chen*

Micro-supercapacitors (MSCs) as a new class of energy storage devices have attracted great attention due to their unique merits. However, the narrow operating voltage, slow frequency response, and relatively low energy density of MSCs are still insufficient. Therefore, an effective strategy to improve their electrochemical performance by innovating upon the design from various aspects remains a huge challenge. Here, surface and structural engineering by downsizing to quantum dot scale, doping heteroatoms, creating more structural defects, and introducing rich functional groups to two dimensional (2D) materials is employed to tailor their physicochemical properties. The resulting nitrogen-doped graphene quantum dots (N-GQDs) and molybdenum disulfide quantum dots (MoS₂-QDs) show outstanding electrochemical performance as negative and positive electrode materials, respectively. Importantly, the obtained N-GQDs//MoS₂-QDs asymmetric MSCs device exhibits a large operating voltage up to 1.5 V (far exceeding that of most reported MSCs), an ultrafast frequency response (with a short time constant of 0.087 ms), a high energy density of 0.55 mWh cm⁻³, and long-term cycling stability. This work not only provides a novel concept for the design of MSCs with enhanced performance but also may have broad application in other energy storage and conversion devices based on QDs materials.

1. Introduction

With the advent of self-powered nanodevices, implantable medical and portable/wearable electronic devices, innovative research toward new energy storage and conversion devices that are small in size, lightweight, flexible, and other matching features has become increasingly important.^[1–7] Among them, micro-supercapacitors (MSCs) are considered as a promising

power source for these emerging modern microelectronic devices because of their impressive advantages such as small dimensions, diversified shapes, good compatibility, superior rate capability, high power density, and long lifespan.^[8,9]

Despite recent progress, the performances of the majority of previously reported MSCs are still insufficient to satisfy the increased demand of the new consumer electronics. It is clear that substantial improvement can be made toward its narrow operating voltages (no more than 1.2 V in aqueous electrolyte), relatively low energy density, slow frequency response capability, and so on.^[10,11] Therefore, much effort has been devoted to improving the electrochemical performance of MSCs by innovating upon their design from various aspects.^[12–18] In particular, the development of advanced electrode materials with excellent electrochemical performance by surface and structural engineering is the most reliable and straightforward strategy because the entire performance of cell is highly dependent on the electrode materials.

Among these surface and structural engineering strategies, the size-minimization strategy is an effective approach in improving the electrochemical performance of electrode materials because the ion transport time (τ) is proportional to the square of the diffusion length L ($\tau \approx L^2/D$).^[19,20] Considering this, the miniaturized electrode materials with small length scales down to several nanometers (such as quantum dots) can significantly reduce ion diffusion distance, create more active sites, and provide large contact area between electrode and electrolyte, which endow them with unique advantages as electrode materials. In addition to decreasing the size of electrode materials, it is highly desirable to incorporate with other surface and structural engineering strategies during the synthesis process to further boost the supercapacitive performance of these electrode materials due to their strong synergistic effects and novel physicochemical properties induced.

2D materials based quantum dots (QDs) derived from their bulk counterparts can not only exhibit enhanced or novel physicochemical and electronic properties due to quantum

W. Liu, M. Zhang, M. Li, B. Li, Dr. W. Zhang, Dr. G. Li, Dr. M. Xiao, Dr. J. Zhu, Prof. A. Yu, Prof. Z. Chen
Department of Chemical Engineering
Waterloo Institute for Nanotechnology
University of Waterloo
Waterloo, Ontario N2L3G1, Canada
E-mail: aipingyu@uwaterloo.ca; zhwenchen@uwaterloo.ca

 The ORCID identification number(s) for the author(s) of this article can be found under <https://doi.org/10.1002/aenm.201903724>.

DOI: 10.1002/aenm.201903724

confinement effects, high surface-to-volume ratio, and structural defects,^[11b,21,22] but also maintain most intrinsic properties and crystalline structure of the corresponding bulk materials in a certain degree.^[11b,21,22] Therefore, 2D materials based QDs could be ideal candidates for electrode materials of MSCs due to their short ion diffusion time, unique layer structure, large effective surface area, and rich edge planes and defects. Nonetheless, there are only a few reports on QDs based electrode materials for electrochemical energy storage devices, not to mention MSCs. Undoubtedly, it is a meaningful but challenging attempt to construct high-performance asymmetric MSCs using 2D materials based QDs. This is expected to not only take full advantage of the merits of the 2D materials based QDs and the synergistic effects between them but also effectively solve the above-mentioned problems associated with MSCs.

In this work, surface and structural engineering accomplished by the reduction of size, the introduction of heteroatom element, and the production of structural defects has been employed to design and prepare defect-enriched nitrogen-doped graphene quantum dots (N-GQDs) and molybdenum disulfide quantum dots (MoS₂-QDs). Owing to their unique advantages, the resulting N-GQDs and MoS₂-QDs exhibit remarkable electrochemical performance as negative and positive electrode materials, respectively. Importantly, the obtained GQDs//MoS₂-QDs asymmetric MSCs display a large potential window (1.5 V), a high volumetric capacitance (1.8 F cm⁻³), a high rate capability (up to 1000 V s⁻¹), a fast frequency response (with a small time constant of 0.087 ms), and a long cycling stability (89.2% retention after 10 000 cycles). These appreciable electrochemical performances are mainly attributed to the respective merits of 2D N-GQDs and MoS₂-QDs, the 3D hierarchical structure assembled as well as the synergistic effect between them.

2. Results and Discussion

2.1. Characterization of Negative Electrode Materials (N-GQDs)

The morphology and detail structure of N-GQDs are characterized by transmission electron microscopy (TEM) and atomic force microscopy (AFM), respectively. From low-resolution TEM images (Figure 1a,b), the resulting N-GQDs have a uniform and narrow distribution with size ranging from 1 to 5 nm (Figure 1c). The N-GQDs (inset of Figure 1b) possess high crystallinity with a lattice spacing of 0.26 nm, which is consistent with the crystalline structure of graphite.^[23] Moreover, as shown by AFM characterization (Figure 1d–f), the thickness of N-GQDs is less than 1.5 nm, suggesting that the as-prepared N-GQDs are 1–3 graphene.^[24] Additionally, X-ray photoelectron spectroscopy (XPS) is used to further study the chemical composition and bonding structure of elements in N-GQDs, with nitrogen-doped graphene nanosheets (N-GNSs) as a reference. XPS survey (Figure S1, Supporting Information) shows the coexistence of C, N, and O elements in the N-GQDs. It is noted that the C1s spectrum is deconvoluted into four peaks, corresponding to C–C (sp² C) at 284.8 eV, C–C (sp³ C) at 286.2 eV, C=O at 287.5 eV, and O=C–O at 288.7 eV, respectively

(Figure 1g). Obviously, the N-GQDs show a larger sp³/sp² ratio (0.63) compared to that of N-GNSs (0.36), indicating the presence of more defects in the resulting N-GQDs.^[25] As shown in Figure 1h, the N1s spectrum is divided into three peaks, which correspond to pyrrolic-N (at 398.6 eV), pyridinic-N (at 400.1 eV), and graphitic-N (at 401.9 eV). It is noted that the relative amount of pyridinic-N in N-GQDs is larger than that in N-GNSs, implying more pseudo-capacitance contribution of N-GQDs as the pyridinic-N is electrochemically reactive.^[26,27] In addition, the O1s spectrum (Figure 1i) is resolved into three peaks, which are assigned to C=O (531.2 eV), C–O (532.6 eV), and O=C–O (533.8 eV), respectively. Here, the residual oxygen functional groups and the incorporation of N into the carbon framework can not only tune the electron/donor characteristics and create more defects but also facilitate the surface wettability and increase the contact area between N-GQDs and electrolyte, thus causing the enhancement of their electrochemical performances due to improved electronic conductivity, more active sites, and fast ions diffusion.^[28–31]

The electrochemical performance of N-GQDs was first investigated by cyclic voltammetry (CV) technique at various scan rates and galvanostatic charge/discharge (GCD) technique. As shown in Figure 2a–c, the CV curves of the N-GQDs at relatively low scan rates exhibit a rectangular shape, showing a typical characteristic of an ideal electric double-layer capacitor of N-GQDs.^[29,32] Particularly, the CV curve (Figure 2d) still maintains a near-rectangle shape without obvious distortion even at 100 V s⁻¹, suggesting an excellent rate capability of the N-GQDs electrode. Notably, the discharge current shows a good linear relationship with scan rates ranging from 0.1 to 100 V s⁻¹ (Figure 2e), revealing a fast ion diffusion and a rapid charge transportation of N-GQDs electrode during the electrochemical process. Meanwhile, its volumetric specific capacitance versus scan rates is displayed in Figure 2f. It is worth mentioning that the volumetric/area specific capacitance is more accurate than that of the gravimetric value to estimate the performance of thin-film electrode as the mass loading of electrode is negligible. Notably, the largest volumetric specific capacitance is about 14.7 F cm⁻³ at 0.1 V s⁻¹, while it still remains as high as 3.3 F cm⁻³ (at 100 V s⁻¹) when the scan rate is increased by a factor of 1000, implying a high-power output capability of N-GQDs electrode. Moreover, the observed nearly linear and symmetric charge/discharge curves (Figure S2, Supporting Information) and no obvious “IR drop” further demonstrate its good capacitive behavior, high columbic efficiency, as well as small equivalent internal resistance. The specific capacitance of N-GQDs obtained from charge/discharge curve at 1.6 A cm⁻³ is about 13.2 F cm⁻³. Additionally, the cycling stability, another critical parameter for evaluating the electrochemical performance of electrode material, is evaluated by CV curve at 1 V s⁻¹. It is observed that the N-GQDs electrode maintains 93% of its initial specific capacitance after 6000 repetitive cycles (Figure S3, Supporting Information), demonstrating its superior cycling life. The outstanding electrochemical performance of the N-GQDs electrode is mainly attributed to the distinctive features of N-GQDs including oxygen-rich functional groups, abundant defects, and good hydrophilicity. These features can provide more active sites, more accessible edges, and large contact area between N-GQDs and electrolyte. Furthermore,

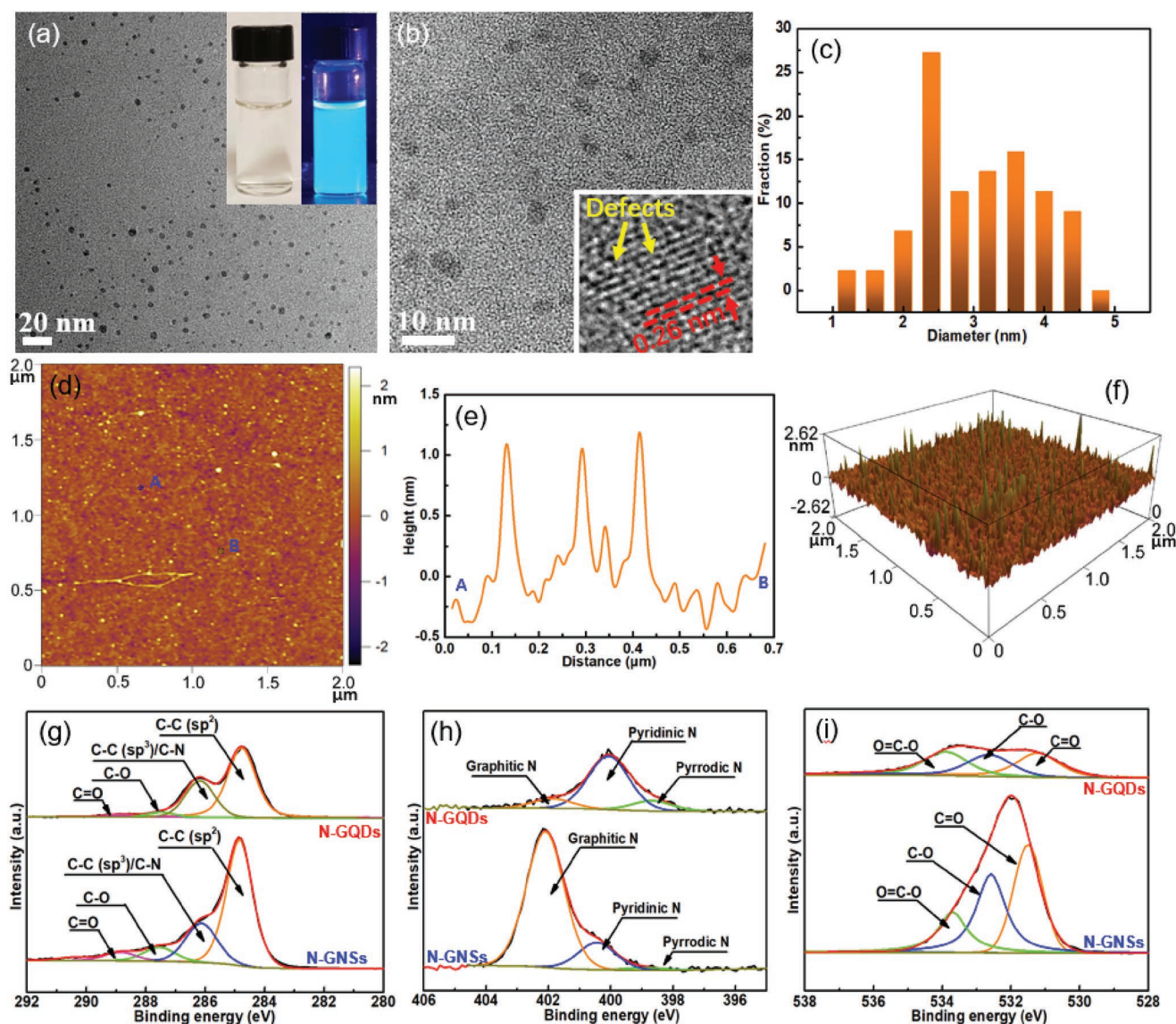


Figure 1. a) Low-resolution TEM image of N-GQDs, b) high-resolution TEM image of N-GQDs (Inset is the HRTEM lattice fringe), and c) its corresponding size distribution. d) AFM image of N-GQDs and its corresponding e) height and f) 3D surface plot of the top view. XPS spectra of N-GQDs: g) C1s, h) N1s, and i) O1s, respectively. Inset in (a) is the photographs of N-GQDs under (left) visible light and (right) UV light, respectively.

its unique 3D interconnected structure assembled, as well as the good contact between N-GQDs and current collector further allow the efficient access of electrolyte, the fast transport of ions/electrons, and the high utilization of the active material.

2.2. Characterization of Positive Electrode Materials (MoS₂-QDs)

The morphology and structure information of the resulting MoS₂-QDs were investigated by different characterization techniques as shown in Figure 3. The low-resolution TEM images (Figure 3a,b) show that the size of MoS₂-QDs is uniform with a narrow size distribution ranging from 1 to 5 nm (Figure 3c). The lattice spacing of MoS₂-QDs is about 0.24 nm (inset of Figure 3b), which is assigned to the (103) plane of the MoS₂ crystal. As shown in the AFM images (Figure 3d–f), the

thickness of the obtained MoS₂-QDs is about 1.5 nm, demonstrating their monolayer or few-layer (about 0.8–1.0 nm) nature. Moreover, X-ray diffraction (XRD) and Raman spectra are performed to evaluate the crystallinity and structure evolution of the MoS₂-QDs as compared to bulk MoS₂. It is noted that the weak (002) diffraction peak and the disappearance of other representative peaks in MoS₂-QDs diffraction pattern indicate that there are no long-range ordered crystal face and a limited portion of the crystalline lattice involved in diffraction, implying the as-prepared MoS₂-QDs with ultrafine size and monolayer or few-layer structure (Figure S4, Supporting Information).^[33–36] Furthermore, the Raman peaks of MoS₂-QDs (Figure S5, Supporting Information) at 380.3 and 405.4 cm⁻¹ are assigned to E¹_{2g} and A¹_g, respectively, and exhibit an apparent blueshift compared to those of bulk MoS₂. This is due to the E¹_{2g} stiffening and A¹_g softening with the decrease of layer thickness.^[37,38]

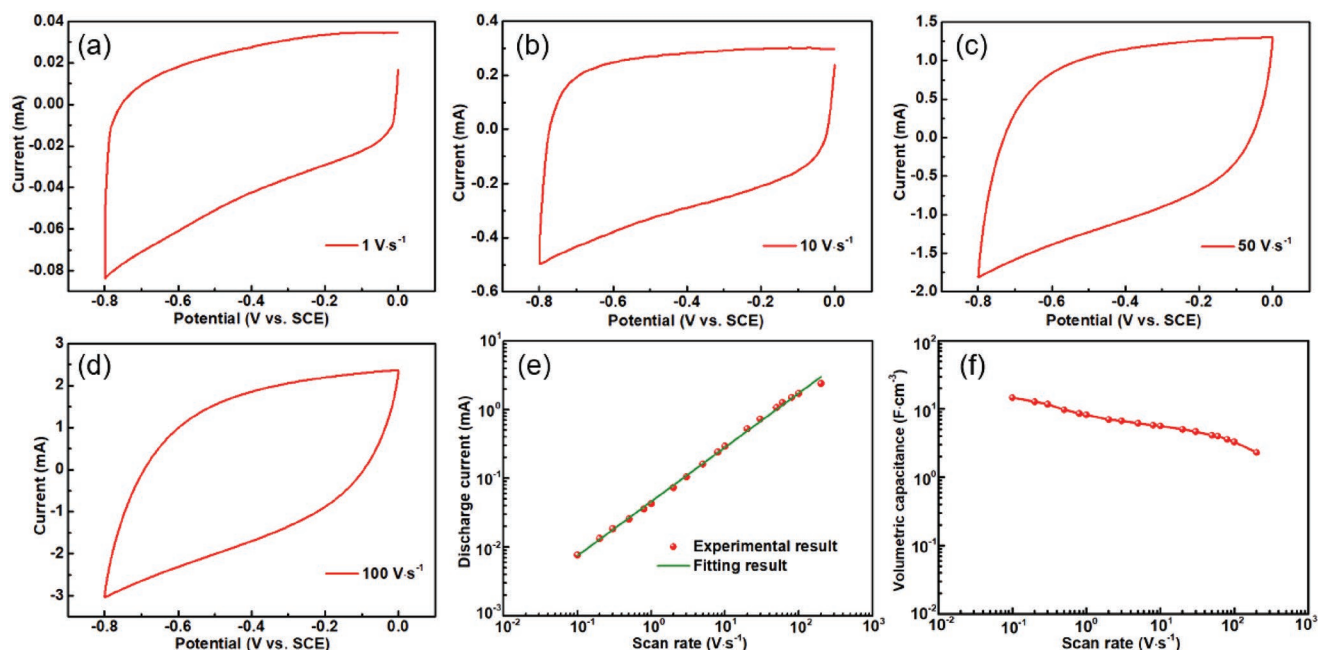
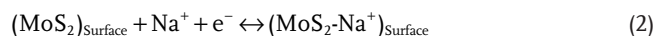


Figure 2. a–d) CV curves of N-GQDs negative electrode in 0.5 M Na₂SO₄ electrolyte at different scan rates: 1, 10, 50, and 100 V s⁻¹, respectively. e, f) Evaluation of the discharge current and volumetric capacitance of N-GQDs negative electrode as a function of scan rates.

XPS is used to further clarify the valence state and chemical composition of the MoS₂-QDs. XPS survey (Figure S6, Supporting Information) confirms the presence of Mo, S, and O elements in the resulting MoS₂-QDs. The high-resolution Mo 3d spectrum (Figure 3g) shows three major peaks at 229.7, 232.9, and 236.1 eV, corresponding to Mo 3d_{5/2}, Mo 3d_{3/2}, and Mo 3d_{3/2}, respectively. This reveals the dominance of the Mo⁺⁴ valence state in the product with the coexistence of the Mo⁺⁵ and Mo⁺⁶ valence states, indicating that there is a slight oxidation of the Mo⁺⁴ ions during the solvothermal reaction.^[34,35,38] Meanwhile, the binding energy of S 2s (Figure 3h) slightly shifts from 227 to 226.6 eV, demonstrating that the S valence state in MoS₂ has been affected by the change of Mo valence state. Moreover, the S 2p spectrum confirms that the existing valence states of S in MoS₂-QDs are S⁻² and S⁺⁶, indicating its small partial oxidation. Notably, the O 1s spectrum (Figure 3i) is divided into three peaks, which are attributed to the Mo–O bond, the surface-adsorbed species (OH⁻, O, or oxygen vacancies), and the adsorbed water, implying a partial oxidation of MoS₂-QDs.^[34,39] Such partial oxidation of MoS₂-QDs can introduce rich defects, thus modify the electronic properties of MoS₂-QDs and produce more active surface area, which benefits to the enhancement of electrochemical performance.

As shown in Figure 4a–c, the CV curves of MoS₂-QDs show a good mirror image with respect to *x*-axis and a rapid current response at each end potential, illustrating a dominant Faradaic pseudo-capacitive behavior accompanying by a non-Faradaic double-layer behavior of MoS₂-QDs. It should be mentioned that the associated energy storage mechanism is proposed as follows^[40,41]



where the Faradaic process (1) is related to the intercalation/deintercalation of Na⁺ into the interlayer structure of MoS₂-QDs, while the non-Faradaic process (2) is assigned to the adsorption/desorption of Na⁺ at the interface of MoS₂-QDs/electrolyte. As the scan rate is up to 100 V s⁻¹, the CV curve still maintains a quasi-rectangular shape (Figure 4d), implying a low resistance and a high reversibility of the intercalation/deintercalation process of MoS₂-QDs electrode. This ultrahigh scan rate of MoS₂-QDs electrode is almost three orders of magnitude larger than those of conventional MoS₂-based SCs,^[41–44] thus demonstrating an excellent rate capability of the MoS₂-QDs electrode. It is noted that there is a good linear dependence between discharge currents and scan rates up to at least 100 V s⁻¹ (Figure 4e), indicating a superfast intercalation/deintercalation process of the MoS₂-QDs electrode. It is noted that its areal specific capacitance gradually decreases from 7.9 to 1.8 F cm⁻² when there is a three orders of magnitude variation in scan rates ranging from 0.1 to 100 V s⁻¹ (Figure 4f). The good linearity and symmetrical triangle of the charge/discharge curve (Figure S7, Supporting Information) further implies good capacitor behavior of MoS₂-QDs electrode. Also, a high specific capacitance of 7.4 F cm⁻³ is achieved according to the charge/discharge curve. Moreover, the MoS₂-QDs electrode shows a long-term cycling stability with 86.5% retention of its initial capacitance after 6000 cycles (Figure S8, Supporting Information), which is much better than those of other reported MoS₂-based nanomaterials: MoS₂/PANI hybrid materials (60.9% retention after 1000 cycles),^[45] MoS₂/RGO@PANI (82.5% retention after 3000 cycles),^[46] and MoS₂/Mn₃O₄ nanostructure (69.3% retention after 2000 cycles).^[47] The superior durability is probably due to its unique 3D structure and the extreme small

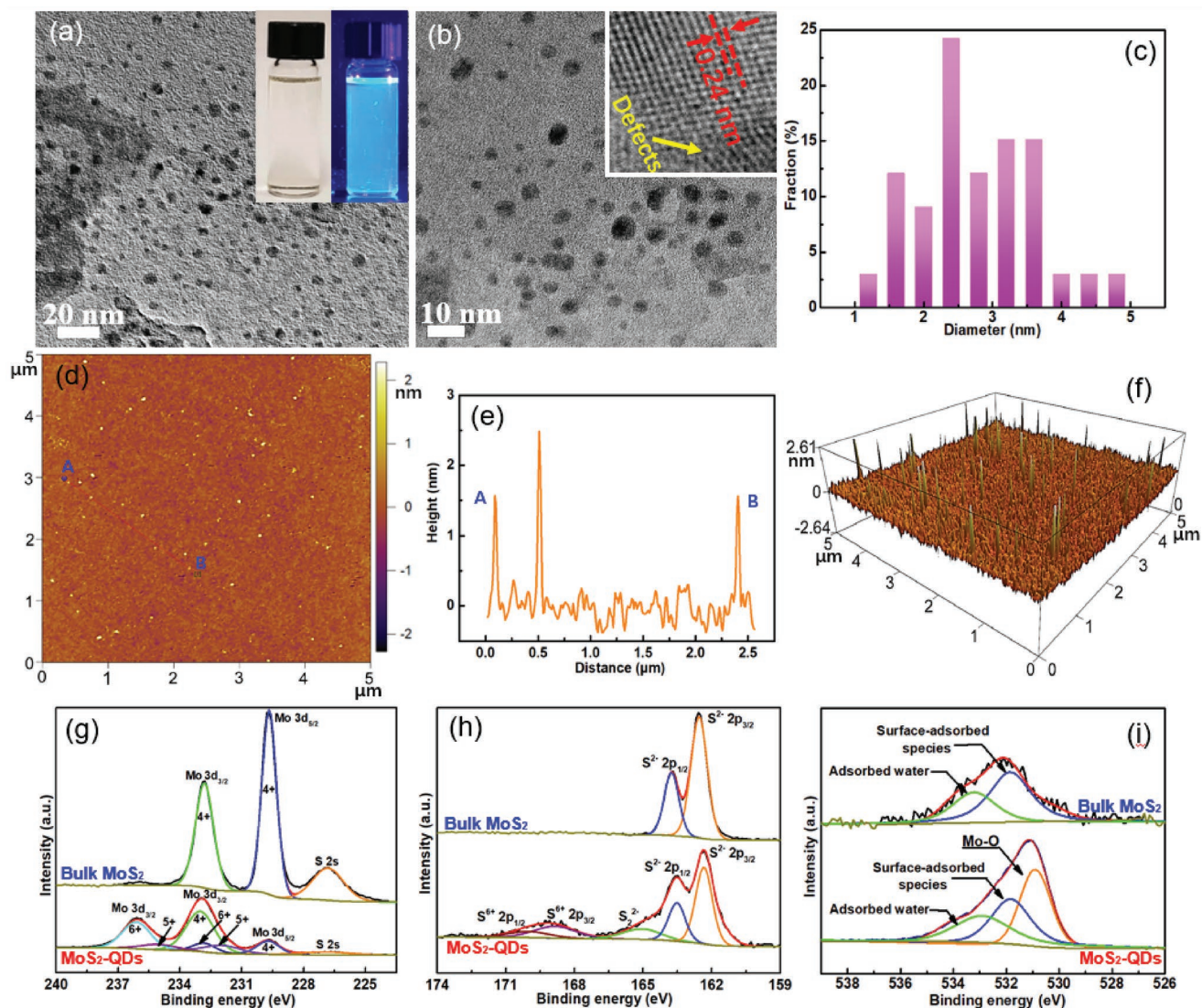


Figure 3. a) Low-resolution TEM image of MoS₂-QDs, b) high-resolution TEM image of MoS₂-QDs, and c) its corresponding size distribution. d) AFM image of MoS₂-QDs and its corresponding e) height and f) 3D surface plot of the top view. g–i) XPS spectra of MoS₂-QDs: Mo 3d, S 2p, and O 1s, respectively. Inset in (a) is the photographs of MoS₂-QDs under (left) visible light and (right) UV light, respectively.

size of MoS₂-QD which can provide a large contact area, effectively shorten the ion diffusion distance, and buffer the volume change during the intercalation/deintercalation processes.^[48] The above electrochemical results indicate that MoS₂-QDs with nanoscale size, high surface area, and enriched defects are promising positive material.

2.3. Characterization of N-GQDs//MoS₂-QDs Asymmetric Micro-Supercapacitors

Inspired by the excellent capacitive behavior of N-GQDs and MoS₂-QDs shown in half-cells, the asymmetric MSCs were successfully constructed with capacitor-type of N-GQDs and battery-type of MoS₂-QDs as negative and positive materials, respectively. In this configuration, a wide potential window can be obtained by taking the advantage of the different stable

potential window of the N-GQDs anode and the MoS₂-QDs cathode as well as their relatively high overpotentials for HER and OER.^[48] The low-magnification scanning electron microscopy (SEM) images (Figure 5a,b) show that the interdigital electrodes are alternately covered by N-GQDs and MoS₂-QDs, both of which exhibit a unique 3D structure, beneficial for easy access of electrolyte and fast transportation of electron/charge. The high-magnification SEM image (Figure 5c) shows that there are many free spaces among the N-GQDs with even a small fraction of N-GQDs agglomeration observed, facilitating the penetration of electrolyte and ensuring the active materials participate in the electrochemical reaction. As shown in the high-magnification SEM image (Figure 5e), there are lots of voids among the MoS₂-QDs produced during the assembling process, which can shorten the diffusion distance of the electrolyte ions and provide more surface-active sites for Faradic redox reaction. In addition, the cross-section SEM images show

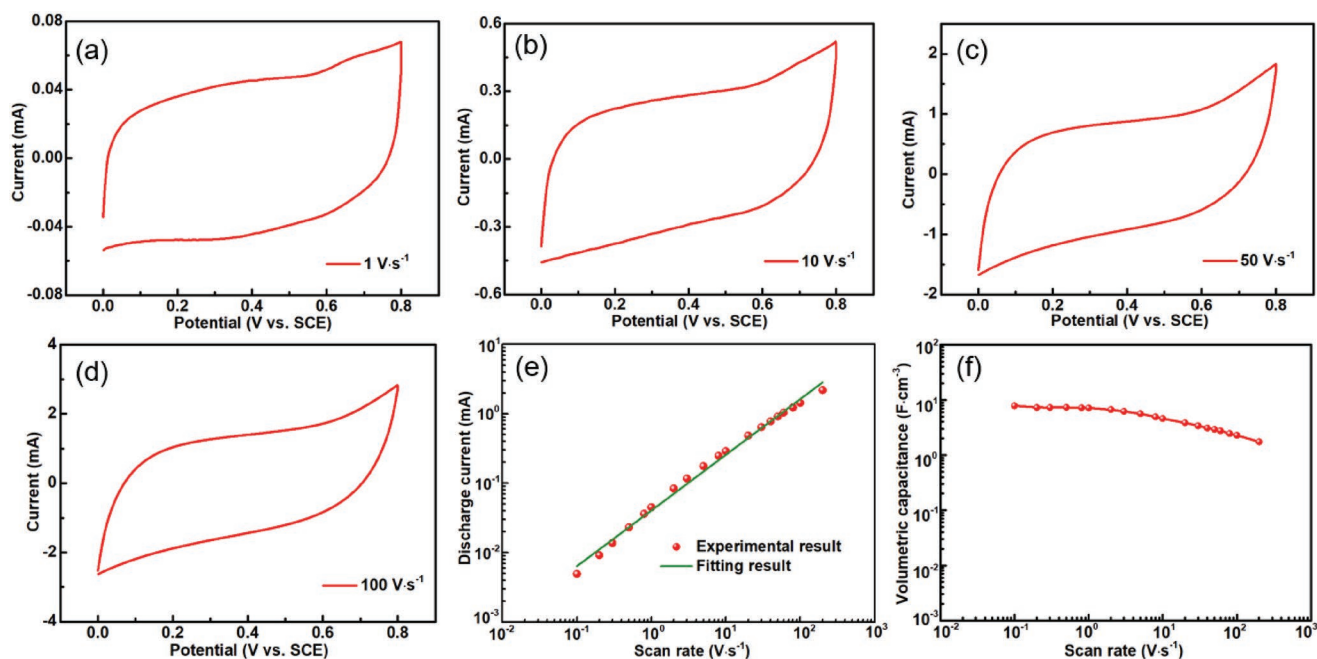


Figure 4. a–d) CV curves of MoS₂-QDs positive electrode in 0.5 M Na₂SO₄ electrolyte at different scan rates: 1, 10, 50, and 100 V s⁻¹, respectively. e,f) Evaluation of the discharge current and volumetric capacitance of MoS₂-QDs negative electrode as a function of the scan rates.

that the thickness of the N-GQDs (Figure 5d) and MoS₂-QDs (Figure 5f) films are about 142 and 171 nm, respectively.

To achieve a large and stable potential window for asymmetric MSCs (Figure 6a), it is crucial to balance the charges between the N-GQDs negative electrode (q⁻) and the MoS₂-QDs positive electrode (q⁺). According to the typical CV curves

of N-GQDs and MoS₂-QDs electrodes (Figure 6b), the ratio of deposition time between the negative material and the positive material is 0.91. The CV curves (Figure 6c) of the as-prepared N-GQDs//MoS₂-QDs asymmetric MSCs maintain a near-rectangular shape when the operating voltage of the device gradually increases from 0.9 to 1.5 V, while it will deviate from the

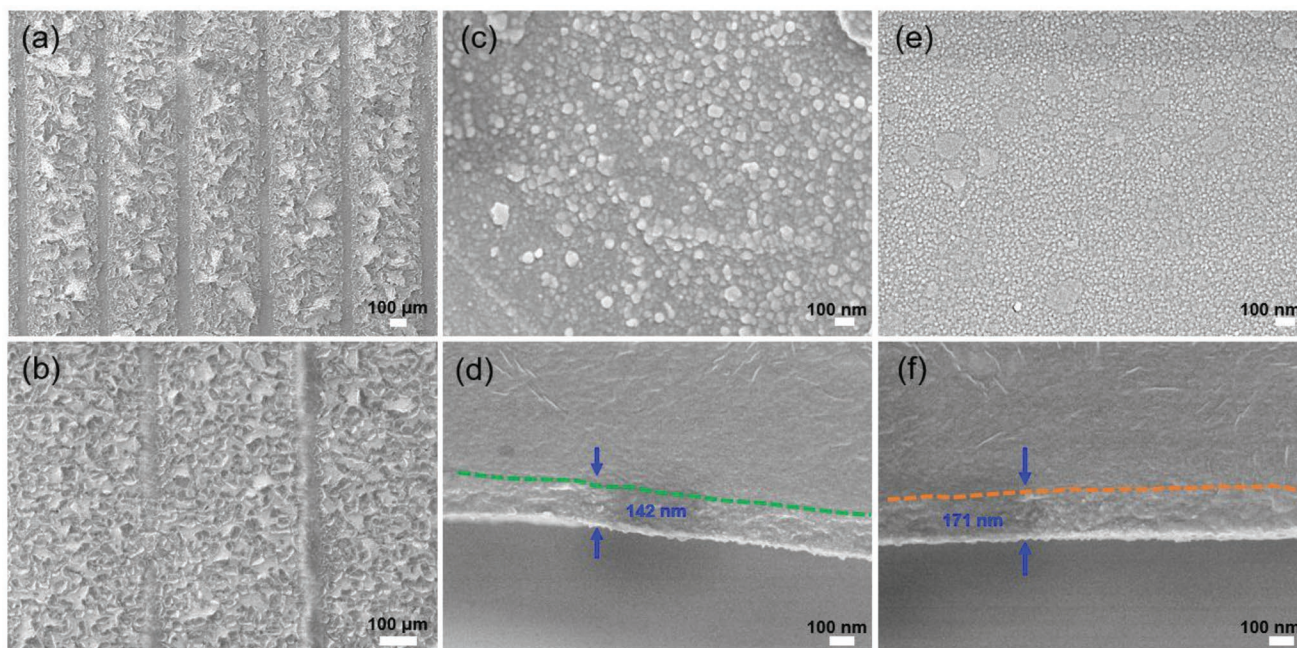


Figure 5. a,b) Low-magnification SEM images of the interdigital finger electrodes after the alternative deposition of N-GQDs and MoS₂-QDs. c) High-magnification SEM of N-GQDs finger electrode and d) its corresponding cross-section image. e) High-magnification SEM image of MoS₂-QDs finger electrode and f) its corresponding cross-section image.

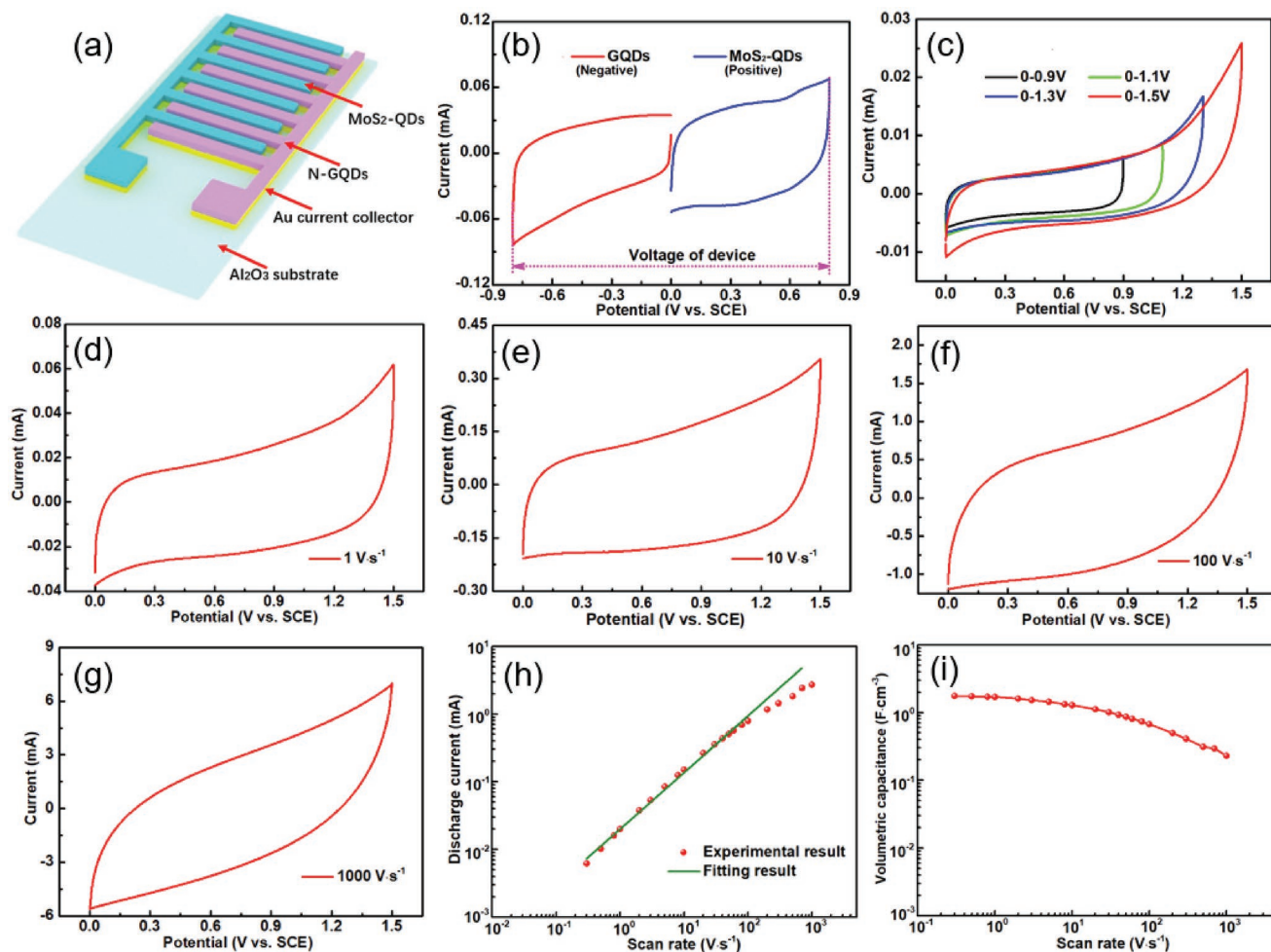


Figure 6. a) Illustration of the as-prepared N-GQDs//MoS₂-QDs asymmetric MSCs. b) Comparative CV curves of N-GQDs and MoS₂-QDs electrodes at 1 V s⁻¹. c) CV curves of the N-GQDs//MoS₂-QDs asymmetric MSCs with different potential windows at 0.3 V s⁻¹. d–g) CV curves of the device measured at different scan rates: 1, 10, 100, and g) 1000 V s⁻¹, respectively. h) Plots of dependence between discharge currents and scan rates. i) Volumetric capacitance of the cell as a function of scan rates ranging from 0.3 to 1000 V s⁻¹.

rectangle shape due to polarization when the potential window is further extended. Furthermore, the energy storage of the device is proportional to the square of the potential window. Based on the above considerations, the operating voltage of the N-GQDs//MoS₂-QDs asymmetric MSCs is set to 1.5 V for further study in the subsequent research. The CV curves (Figure 6d–f) show a near perfect rectangle shape and no observable redox peaks when the scan rates are below 100 V s⁻¹, indicating a typical capacitive behavior of the MSCs with fast ion diffusion and rapid electron transportation. Importantly, the CV curve (Figure 6g) retains a nearly rectangle-shaped profile with slight distortion even at an ultrahigh scan rate of 1000 V s⁻¹, which implies a small equivalent series resistance and an excellent rate capability of the microdevice. Remarkably, this ultrahigh scan rate is close to three orders of magnitude higher than those of conventional supercapacitors, and higher or comparable to those of reported MSCs based on onion-like carbon (200 V s⁻¹),^[49] electrochemically reduced graphene oxide (400 V s⁻¹),^[50] plasma reduced graphene (1000 V s⁻¹),^[51] and vertically aligned CNTs (1000 V s⁻¹).^[52] It is noted that the

discharge currents show a linear dependence with the scan rates below 200 V s⁻¹ (Figure 6h), implying a fast surface-controlled kinetics; while with further increase of the scan rates, the linear relationship slightly deviates due to ohmic resistance. Impressively, a maximum volumetric capacitance of 1.8 F cm⁻³ is achieved at 0.3 V s⁻¹ as shown in Figure 6i. This value is larger than or comparable to those of reported MSCs based on different materials: graphene/CNTs (1.08 F cm⁻³),^[53] onion-like carbon (1.10 F cm⁻³),^[49] laser reduction graphene (3.10 F cm⁻³),^[54] and reduced graphene oxide/MnO₂/AgNW (4.42 F cm⁻³).^[9] Furthermore, the Ragone plots, which display the volumetric energy and power densities of N-GQDs//MoS₂-QDs asymmetric MSCs compared with other reported MSCs and commercial energy storage devices, are shown in Figure S9 (Supporting Information). Remarkably, the N-GQDs//MoS₂-QDs asymmetric MSCs show a volumetric energy density of 0.55 mWh cm⁻³, which is comparable to or larger than other reported MSCs such as laser-scribed graphene,^[1,54] laser scribed graphene/carbon nanotubes (CNTs),^[55] graphene/CNTs,^[53] graphene oxide/CNTs hybrid,^[56] and reduced

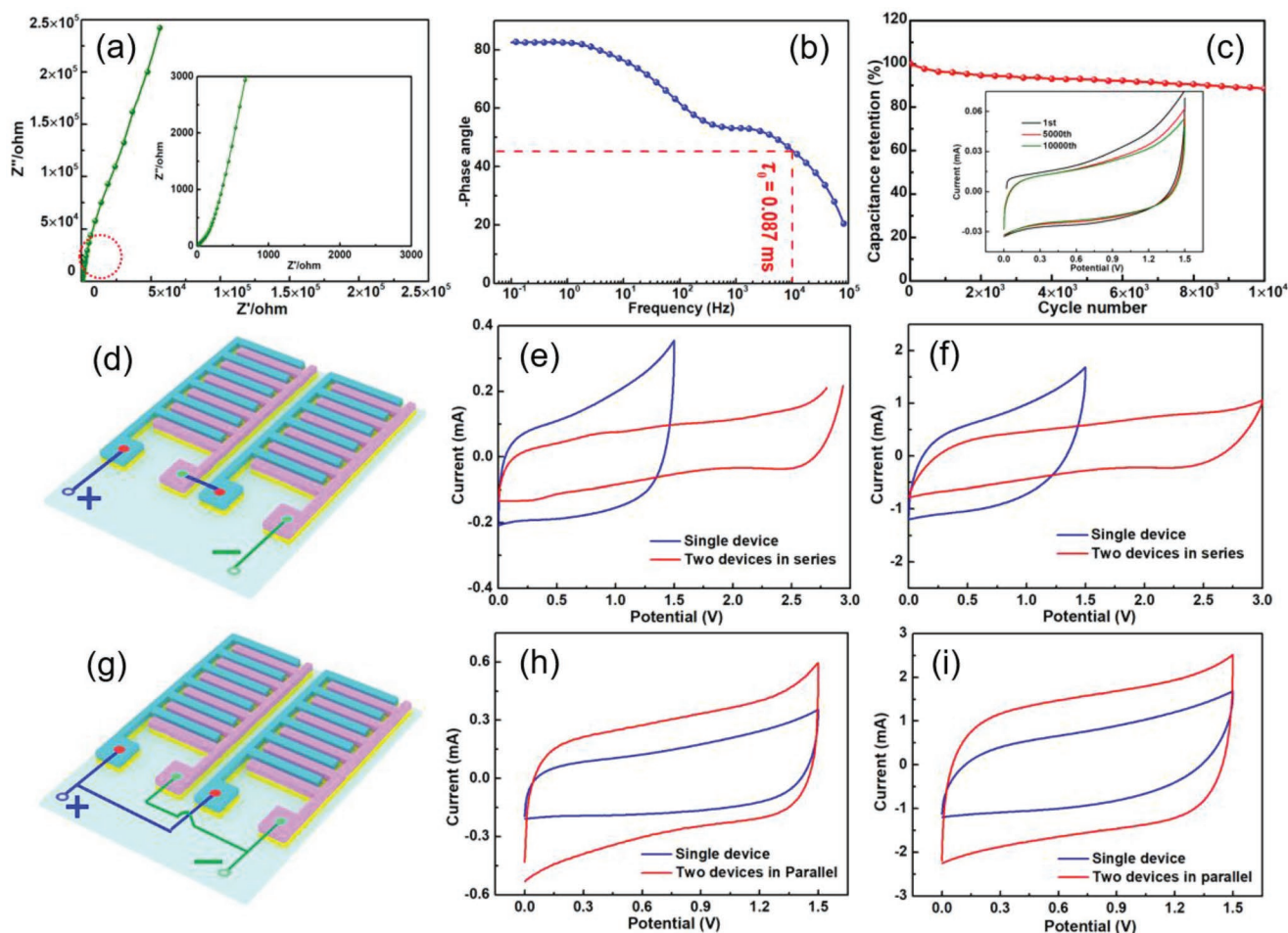


Figure 7. a) Nyquist plot of the MSCs showing the imaginary part versus the real part. b) Plot of impedance phase angle versus frequency. c) Capacitance retention of the MSCs as a function of cycle number measured at the scan rate of 1 V s^{-1} with 10 000 cycles. d) Illustration of two MSCs connected in series and corresponding CV curves: e) 10 V s^{-1} , f) 100 V s^{-1} . g) Illustration of two MSCs connected in parallel and corresponding CV curves: e) 10 V s^{-1} , f) 100 V s^{-1} .

graphene oxide/ MnO_2/AgNW .^[9] Particularly, this energy density is about two orders of magnitude larger than that of commercial electrolytic capacitors and comparable to that of thin-film lithium-ion batteries.^[1,49,54]

Electrochemical impedance spectrometry (EIS) is carried out to further characterize the MSCs and reveal the underlying reason behind its excellent electrochemical performance. As shown in **Figure 7a**, the Nyquist plot show a near-straight line along the imaginary axis and no obvious semicircle is observed, suggesting a near-capacitive behavior and a small resistance of the resulting MSCs. Moreover, the relaxation time constant ($\tau_0 = 1/f_0$), another key factor of MSCs associated with diffusion manifested at low frequencies, is a quantitative evaluation of how fast the cell discharge all energy with efficiency more than 50%. The smaller value of the relaxation time constant, the faster power response capability of the MSCs. The relaxation time constant (τ_0) of the resulting N-GQDs// MoS_2 -QDs asymmetric MSCs is 0.087 ms (Figure 7b), which is three orders of magnitude smaller than those of conventional double-layer capacitors (1 s) and much lower than those of most reported MSCs based on onion-like carbon (26 ms),^[49]

sulfuric-acid-treated poly(3,4-ethylenedioxythiophene):poly(styrenesulfonate) (0.588 ms),^[57] plasma-reduced graphene (0.28 ms),^[51] and electrochemically reduced graphene oxide (0.17–1 ms).^[50] This result indicates a fast power response capability and a promising potential of the as-prepared device in the filtering application. Furthermore, another important aspect for the evaluation of MSCs is the long-term cycling stability, which is performed by continuous CV testing. Notably, there is still 89.2% retention of its initial capacity after 10 000 cycles (Figure 7c), suggesting a good cycling stability. TEM characterization (Figure S10, Supporting Information) is carried out to check the structure change of the samples after the cycling test. It can be observed that both N-GQDs and MoS_2 -QDs can well maintain their structure without apparent changes, indicating good mechanical and electrochemical stability. Therefore, it is reasonable to deduce that the capacitance decay presented here is probably from the slight volume change of battery-type based material of MoS_2 -QDs and the existence of side reaction occurring at the electrode/electrolyte interface in the large potential window. Additionally, in order to meet certain requirements of consumer electronic devices, it is necessary to connect two

devices in series and parallel configuration (Figure S11, Supporting Information) to extend operating voltage and increase capacitance, respectively. As shown in Figure 7d–f, the operating voltage of two devices connected in series is double compared to that of single cell, which indicates that the prepared devices are with a high consistency and obey the rule of series connection of capacitor. Importantly, the device keeps a rectangular shape even at 100 V s^{-1} , demonstrating an excellent rate capability. Moreover, when two MSCs are connected in parallel (Figure 7g–i), the current is almost two times larger than that of a single MSC, suggesting it follows the principle of parallel connection of capacitor. In addition, the CV curve retains a near-rectangular shape at 100 V s^{-1} , further revealing the superior rate capability.

The excellent electrochemical performance of the N-GQDs// MoS_2 -QDs asymmetric MSCs is by virtue of the following advantages derived from the special physicochemical properties of N-GQDs and MoS_2 -QDs, the synergistic effect between them, and their unique 3D structures assembled. First, the N-GQDs negative electrode maintains the distinctive features of N-GQDs including large active surface area, good hydrophilicity, and large contact area between electrode and electrolyte, which endow them with unique advantages as electrode materials. Also, the formed 3D hierarchical structure facilitates the easy access of electrolyte, benefits to the rapid transport of electrolyte ions, and accelerates the fast transport of electron. Second, the MoS_2 -QDs positive electrode not only retains the merits of MoS_2 -QDs such as two-dimensional layered crystal structure, high specific capacitance, and more accessible edge sites, but also possesses a unique 3D hierarchical architecture. These advantages of MoS_2 -QDs electrode provide a large amount of electrochemical active sites, reduce ion diffusion distance, improve electron transportation from active materials to current collector, and promote fast and reversible intercalation/deintercalation process. Furthermore, the asymmetric configuration of MSCs proposed here can significantly increase energy density (due to the increase of the operating voltage) and still maintain excellent rate capability and long lifespan, which is mainly due to the synergistic effect between battery-type MoS_2 -QDs electrode and capacitor-type N-GQDs electrode.

3. Conclusions

In summary, surface and structural engineering achieved by downsizing to quantum dot scale, doping heteroatom element, creating more structural defect, and introducing rich functional group to 2D materials was employed to prepare defect-enriched N-GQDs and MoS_2 -QDs. By integrating the features of N-GQDs and MoS_2 -QDs as well as the synergistic effect between them, the novel asymmetric MSCs are designed and constructed with capacitor-type N-GQDs as negative electrode and battery-type MoS_2 -QDs as positive electrode. Particularly, the obtained MSCs display outstanding electrochemical performance compared to other reported MSCs, including a high energy density, an excellent rate capability, a fast frequency response capability, and a long-term cycling stability. The study presented here provides a new insight for the construction of high-performance MSCs, and, more importantly, offers a new

reference in designing other high-performance energy storage devices based on 2D materials QDs.

Supporting Information

Supporting Information is available from the Wiley Online Library or from the author.

Acknowledgements

The authors gratefully appreciate the support from the Natural Sciences and Engineering Research Council of Canada (NSERC), University of Waterloo, and Waterloo Institute for Nanotechnology.

Conflict of Interest

The authors declare no conflict of interest.

Keywords

electrode materials, engineering, molybdenum disulfide quantum dots, nitrogen-doped graphene quantum dots, supercapacitors

Received: November 12, 2019

Revised: December 9, 2019

Published online:

- [1] M. F. El-Kady, V. Strong, S. Dubin, R. B. Kaner, *Science* **2012**, 335, 1326.
- [2] Z.-S. Wu, Y.-Z. Tan, S. Zheng, K. Parvez, J. Qin, X. Shi, C. Sun, X. Bao, X. Feng, K. Mullen, *J. Am. Chem. Soc.* **2017**, 139, 4506.
- [3] C. Couly, M. Alhabeb, K. L. Van Aken, N. Kurra, L. Gomes, A. M. Navarro-Suárez, B. Anasori, H. N. Alshareef, Y. Gogotsi, *Adv. Electron. Mater.* **2018**, 4, 1700339.
- [4] K. Lee, H. Lee, Y. Shin, Y. Yoon, D. Kim, H. Lee, *Nano Energy* **2016**, 26, 746.
- [5] X. Pu, M. Liu, L. Li, S. Han, X. Li, C. Jiang, C. Du, J. Luo, W. Hu, Z. L. Wang, *Adv. Energy Mater.* **2016**, 6, 1601254.
- [6] J. W. Long, B. Dunn, D. R. Rolison, H. S. White, *Chem. Rev.* **2004**, 104, 4463.
- [7] M. Armand, J.-M. Tarascon, *Nature* **2008**, 451, 652.
- [8] a) X. Shi, S. Pei, F. Zhou, W. Ren, H.-M. Cheng, Z.-S. Wu, X. Bao, *Energy Environ. Sci.* **2019**, 12, 1534; b) W.-W. Liu, Y. Feng, X. Yan, J. Chen, Q. Xue, *Adv. Funct. Mater.* **2013**, 23, 4111.
- [9] a) W. Liu, C. Lu, X. Wang, R. Y. Tay, B. K. Tay, *ACS Nano* **2015**, 9, 1528; b) J. Chang, S. Adhikari, T. H. Lee, B. Li, F. Yao, D. T. Pham, V. T. Le, Y. H. Lee, *Adv. Energy Mater.* **2015**, 5, 1500003.
- [10] a) Y.-Y. Peng, B. Akuzum, N. Kurra, M.-Q. Zhao, M. Alhabeb, B. Anasori, E. C. Kumbur, H. N. Alshareef, M.-D. Gerc, Y. Gogotsi, *Energy Environ. Sci.* **2016**, 9, 2847; b) W. Liu, X. Yan, J. Chen, Y. Feng, Q. Xue, *Nanoscale* **2013**, 5, 6053.
- [11] a) Q. Jiang, N. Kurra, K. Maleski, Y. Lei, H. Liang, Y. Zhang, Y. Gogotsi, H. N. Alshareef, *Adv. Energy Mater.* **2019**, 9, 1901061; b) S. Das, R. Ghosh, D. Mandal, A. K. Nandi, *ACS Appl. Energy Mater.* **2019**, 2, 6642.
- [12] X. Shi, Z.-S. Wu, J. Qin, S. Zheng, S. Zheng, S. Wang, F. Zhou, C. Sun, X. Bao, *Adv. Mater.* **2017**, 29, 1703034.
- [13] W. Liu, C. Lu, H. Li, R. Y. Tay, L. Sun, X. Wang, W. L. Cow, X. Wang, B. K. Tay, Z. Chen, J. Yan, K. Feng, G. Lui, R. Tjandra, L. Rasenthiram, G. Chiu, A. Yu, *J. Mater. Chem. A* **2016**, 4, 3754.

- [14] W. Si, C. Yan, Y. Chen, S. Oswald, L. Han, O. G. Schmidt, *Energy Environ. Sci.* **2013**, *6*, 3218.
- [15] A. Ferris, S. Garbarino, D. Guay, D. Pech, *Adv. Mater.* **2015**, *27*, 6625.
- [16] L. Zhang, D. DeArmond, N. T. Alvarez, R. Malik, N. Oslin, C. McConnell, P. K. Adusei, Y.-Y. Hsieh, V. Shanov, *Small* **2017**, *13*, 1603114.
- [17] S. Wang, Z.-S. Wu, S. Zheng, F. Zhou, C. Sun, H.-M. Chen, X. Bao, *ACS Nano* **2017**, *11*, 4283.
- [18] J. Pu, X. Wang, R. Xu, K. Komvopoulos, *ACS Nano* **2016**, *10*, 9306.
- [19] H. Zhang, X. Yu, P. V. Braun, *Nat. Nanotechnol.* **2011**, *6*, 277.
- [20] K. Cao, L. Jiao, W. K. Pong, H. Liu, T. Zhou, Z. Guo, Y. Wang, H. Yaun, *Small* **2016**, *12*, 2991.
- [21] Y. Xu, X. Wang, W. L. Zhang, F. Lv, S. Guo, *Chem. Soc. Rev.* **2018**, *47*, 586.
- [22] a) X. Wang, G. Sun, N. Li, P. Chen, *Chem. Soc. Rev.* **2016**, *45*, 2239; b) J. Zhu, A. S. Childress, M. Karakaya, S. Dandeliya, A. Srivastava, Y. Lin, A. M. Rao, R. Podila, *Adv. Mater.* **2016**, *28*, 7185.
- [23] W. W. Liu, J. N. Wang, *Chem. Commun.* **2011**, *47*, 6888.
- [24] S. Lin, L. Dong, J. Zhang, H. Lu, *Chem. Mater.* **2016**, *28*, 2138.
- [25] S. Sarkar, D. Gandla, Y. Venkatesh, P. R. Bangal, S. Ghosh, Y. Yang, S. Misra, *Phys. Chem. Chem. Phys.* **2016**, *18*, 21278.
- [26] J. Han, G. Xu, B. Ding, J. Pan, H. Dou, D. R. MacFarlane, *J. Mater. Chem. A* **2014**, *2*, 5352.
- [27] D.-W. Wang, F. Li, L.-C. Yin, X. Lu, Z.-G. Chen, I. R. Gentle, G. Q. Lu, H.-M. Chen, *Chem. - Eur. J.* **2012**, *18*, 5345.
- [28] T. Shao, G. Wang, X. An, S. Zhou, Y. Xia, C. Zhu, *RSC Adv.* **2014**, *4*, 47977.
- [29] J. Chang, M. Jin, F. Yao, T. H. Kim, V. T. Le, H. Yue, F. Gunes, B. Li, A. Ghosh, S. Xie, Y. Lee, *Adv. Funct. Mater.* **2013**, *23*, 5074.
- [30] N. Soin, S. S. Roy, S. Sharma, T. Thundat, J. A. McLaughlin, *J. Solid State Electrochem.* **2013**, *17*, 2139.
- [31] L.-F. Chen, X.-D. Zhang, H.-W. Liang, M. Kong, Q. F. Guan, P. Chen, Z.-Y. Wu, S.-H. Yu, *ACS Nano* **2012**, *6*, 7092.
- [32] Q. Wang, J. Yan, Y. Wang, T. Wei, M. Zhang, X. Jing, Z. Fan, *Carbon* **2014**, *67*, 119.
- [33] S. Xu, D. Li, P. Wu, *Adv. Funct. Mater.* **2015**, *25*, 1127.
- [34] G. Ou, P. Fan, X. Ke, Y. Xu, K. Huang, H. Wei, W. Yu, H. Zhang, M. Zhong, H. Wu, Y. Li, *Nano Res.* **2018**, *11*, 751.
- [35] W. Gu, Y. Yan, X. Cao, C. Zhang, C. Ding, Y. Xian, *J. Mater. Chem. B* **2016**, *4*, 27.
- [36] D. Gopalakrishnan, D. Damien, M. M. Shaijumon, *ACS Nano* **2014**, *8*, 5297.
- [37] Y. Xu, L. Yan, H. Xu, *Sci. Rep.* **2019**, *9*, 2931.
- [38] W. Gu, Y. Yan, C. Zhang, C. Ding, Y. Xian, *ACS Appl. Mater. Interfaces* **2016**, *8*, 11272.
- [39] T. Zhao, Z. Xing, Z. Xiu, Z. Li, S. Yang, W. Zhou, *ACS Appl. Mater. Interfaces* **2019**, *11*, 7104.
- [40] A. Ramadoss, T. Kim, G.-S. Kim, S. J. Kim, *New J. Chem.* **2014**, *38*, 2379.
- [41] M. Acerce, D. Voiry, M. Chhowalla, *Nat. Nanotechnol.* **2015**, *10*, 313.
- [42] L. Gao, S. Yang, W. Gao, Z. Liu, Y. Gong, L. Ma, G. Shi, S. Lei, Y. Zhang, S. Zhang, R. Vajtai, P. M. Ajayan, *Small* **2013**, *9*, 2905.
- [43] Y. Yang, H. Fei, G. Ruan, C. Xiang, J. M. Tour, *Adv. Mater.* **2014**, *26*, 8163.
- [44] M. A. Bissett, I. A. Kinloch, R. A. W. Dryfe, *ACS Appl. Mater. Interfaces* **2015**, *7*, 17388.
- [45] L. Ren, G. Zhang, Z. Yan, L. Kang, H. Xu, F. Shi, Z. Lei, Z.-H. Liu, *ACS Appl. Mater. Interfaces* **2015**, *7*, 28294.
- [46] X. Li, C. Zhang, S. Xin, Z. Yang, Y. Li, D. Zhang, P. Yao, *ACS Appl. Mater. Interfaces* **2016**, *8*, 21373.
- [47] M. Wang, H. Fei, P. Zhang, L. Yin, *Electrochim. Acta* **2016**, *209*, 389.
- [48] a) V. Bonu, B. Gupta, S. Chandra, A. Das, S. Dhara, A. K. Tyagi, *Electrochim. Acta* **2016**, *203*, 230; b) M. Yu, Y. Lu, H. Zheng, X. Lu, *Chem. - Eur. J.* **2018**, *24*, 3639; c) Y. Shao, M. F. El-Kady, J. Sun, Y. Li, Q. Zhang, M. Zhu, H. Wang, B. Dunn, R. B. Kaner, *Chem. Rev.* **2018**, *118*, 9233.
- [49] D. Pech, M. Brunet, H. Durou, P. Huang, V. Mochalin, Y. Gogotsi, P.-L. Taberna, P. Simon, *Nat. Nanotechnol.* **2010**, *5*, 651.
- [50] K. Sheng, Y. Sun, C. Li, W. Yaun, G. Shi, *Sci. Rep.* **2012**, *2*, 247.
- [51] Z.-S. Wu, K. Parvez, X. Feng, K. Müllen, *Nat. Commun.* **2013**, *4*, 2487.
- [52] A. Ghosh, V. T. Le, J. J. Bae, Y. H. Lee, *Sci. Rep.* **2013**, *3*, 2939.
- [53] J. Lin, C. G. Zhang, Z. Yan, Y. Zhu, Z. W. Peng, R. H. Hauge, D. Natelson, J. M. Tour, *Nano Lett.* **2013**, *13*, 72.
- [54] M. F. El-Kady, R. B. Kaner, *Nat. Commun.* **2013**, *4*, 1475.
- [55] F. S. Wen, C. X. Hao, J. Y. Xiang, L. M. Wang, H. Hou, Z. B. Su, W. T. Hu, Z. Y. Liu, *Carbon* **2014**, *75*, 236.
- [56] M. Beidaghi, C. L. Wang, *Adv. Funct. Mater.* **2012**, *22*, 4501.
- [57] M. Zhang, Q. Zhou, J. Chen, X. Yu, L. Huang, Y. Li, C. Li, G. Shi, *Energy Environ. Sci.* **2016**, *9*, 2005.